ROYAL SOCIETY OF CHEMISTRY

PAPER

Plasmon-induced electron injection into the large negative potential conduction band of Ga_2O_3 for coupling with water oxidation†

Yaguang Wang,[a] Xu Shi,[a] Tomoya Oshikiri, [ID][a] Shuai Zu,[a] Kosei Ueno [ID][b] and Hiroaki Misawa [ID]*[a,c]

In this study, an interfacial modification layer was applied to improve the plasmon-induced light energy conversion of a gallium(III) oxide (Ga_2O_3) photoelectrode, which possesses a much more negative conduction band potential compared with the reduction potential of photons to hydrogen. The plasmon-induced photocurrent generation under visible light irradiation was observed with Au nanoparticle-loaded Ga_2O_3 (Au-NPs/Ga_2O_3). An interfacial modification was carried out by depositing a titanium dioxide (TiO_2) thin-film layer on Au-NPs/Ga_2O_3 *via* atomic layer deposition. Since the surface states of TiO_2 possess excellent hole-trapping ability, this interfacial modification remarkably improved the generation of plasmon-induced photocurrent in the visible region. The photoelectric conversion efficiency of interfacially modified Au-NPs/Ga_2O_3 showed a TiO_2 thin-film thickness dependence because the migration of hot carriers was suppressed with increasing TiO_2 thickness. The Au-NPs/Ga_2O_3 photoelectrode modified with 2 nm-thick TiO_2 showed the best photoelectric conversion performance, and the thermodynamic energy conversion efficiency under irradiation with 600 nm light was approximately two times larger than that of the Au-NPs/TiO_2-thin film due to the extremely negative onset potential of Au-NPs/Ga_2O_3 with TiO_2. Therefore, the plasmonic Ga_2O_3 photoanode with the interfacial TiO_2 modification could provide both a high reduction ability for H_2 evolution and an oxidation ability for water oxidation, because of the negative conduction band of Ga_2O_3 and the hole-trapping property from TiO_2, respectively.

Introduction

Solar water splitting to produce H_2 is a main topic in artificial photosynthesis. To achieve efficient overall water splitting, one indispensable condition is that the bottom of the conduction band (CB) of the semiconductor should be more negative than the reduction potential of H^+/H (0 V *vs.* RHE).[1,2] Therefore, gallium(III) oxide (Ga_2O_3), which possesses a negative CB (−1.0 to −1.5 V *vs.* RHE), is a promising photocatalyst for overall water splitting.[3–6] The largely negative CB potential of Ga_2O_3 can also be applied to the reduction of carbon dioxide to CO or HCOOH.[7] However, it is only able to utilize the ultraviolet

light of solar radiation due to its wide band gap (~4.9 eV).[8] Band engineering is a standard method for extending the absorption edge of a material. Kudo *et al.* reported that doping In_2O_3 into β-Ga_2O_3 to form a solid solution could efficiently shift the absorption edge towards longer wavelengths, thus maintaining H_2 and O_2 evolution.[9] Although the absorption edge can be shifted to longer wavelengths by the doping method, the visible light energy is still insufficiently utilized. Moreover, doping causes a positive shift in the CB, thereby decreasing the reduction potential of Ga_2O_3. Although other methods, such as the addition of cocatalysts and promotors, have also been applied to increase the catalytic performance of Ga_2O_3, the results are not ideal for the use of visible light.[10–12]

Recently, localized surface plasmon resonance (LSPR) of noble metal nanoparticles (Au, Ag) has been increasingly studied because it can efficiently increase visible-light absorption and significantly enhance the electromagnetic near-field.[13–15] Under LSPR excitation, hot carriers are generated in the metal nanoparticles.[16] When settling metal nanoparticles on a semiconductor, a Schottky barrier forms at the interface, and hot carriers with energy higher than the Schottky barrier can transfer to the CB of the semiconductor, thus achieving

[a]*Research Institute for Electronic Science, Hokkaido University, Sapporo, Japan.*
E-mail: misawa@es.hokudai.ac.jp
[b]*Department of Chemistry, Faculty of Science, Hokkaido University, Sapporo, Japan*
[c]*Center for Emergent Functional Matter Science, National Chiao Tung University, Hsinchu, Taiwan*
†Electronic supplementary information (ESI) available: Description of fabrication schematic. Morphology of Au-NPs. Near-field spectrum of different size of Au-NPs. *I–V*, *I–t* and Mott–Schottky curves. Schematic of charge transfer. See DOI: 10.1039/d0nr06319c

charge separation at the interface.[17,18] The electrons transferred to the CB of the semiconductor take part in the reduction reactions, such as H_2 evolution, while the holes will be captured at the surface states of the semiconductor and participate in the oxidation reactions.[19] Importantly, it is expected that this plasmon-induced electron transfer mechanism will not cause a positive shift in the CB of gallium oxide and that visible light will be used effectively while maintaining a high reduction ability.

In plasmon-induced artificial photosynthesis systems using n-type semiconductors, the reducing ability can be improved by changing the type of semiconductor; however, the important point is that it is necessary to efficiently induce water oxidation as the rate-determining step. First, to stably oxidize water for a long time, it is necessary to use an oxide semiconductor in which the photoanode itself is not further oxidized. Second, the surface condition of the photoanode that can efficiently capture holes is required. Recently, we successfully demonstrated that plasmon-induced water oxidation is highly sensitive to the surface states of the crystal facets of $SrTiO_3$, and Au nanoparticle-loaded $SrTiO_3$ that is terminated with a TiO_2 layer shows a high oxidation ability.[20] In addition, Murakoshi et al. also reported that TiO_2 was beneficial for water oxidation by studying the intermediate species during plasmon-induced oxygen evolution.[21] Therefore, improving the hole-trapping ability at the interface by the surface states of TiO_2 is an efficient way to enhance the water oxidation efficiency.

In this study, plasmonic Au-NPs were decorated on the surface of single-crystal Ga_2O_3 (Au-NPs/Ga_2O_3) to utilize visible light without shifting its negative CB energy level, which is beneficial for reduction reactions, such as H_2 evolution. To improve the water oxidation reaction of the Au-NPs/Ga_2O_3 photoelectrode, we also proposed an interfacial modification using a thin TiO_2 layer with a nanometre-scale thickness that was deposited on Au-NPs/Ga_2O_3 by the atomic layer deposition (ALD) technique. Photocatalytic reactivities were evaluated by monitoring the photocurrent of the photoelectrochemical (PEC) reaction. Based on the excellent hole-trapping ability of the as-prepared material, the plasmon-induced holes are efficiently trapped in the surface states at the interfacial boundary between the Au-NPs and TiO_2 layer, which improves the water oxidation reactivity of the Au-NPs/Ga_2O_3 photoelectrode.

Results and discussion

To optimize the conditions for the plasmonic PEC reaction enhancement of Au-NP-loaded Ga_2O_3, we first investigated the particle size effect of Au-NPs loaded on Ga_2O_3 because the LSPR properties of Au-NPs were very sensitive to their size.[22,23] Au-NPs with mean sizes ranging from 10 to 50 nm were fabricated on Ga_2O_3 by annealing Au films with various thicknesses, as depicted in Fig. S1.† Fig. 1a shows the extinction spectra of Au-NPs with different sizes loaded on Ga_2O_3. The LSPR peaks showed an obvious red-shift and a broadening of

Fig. 1 (a) Extinction and (b) IPCE spectra of differently sized Au-NPs loaded on Ga_2O_3.

the full width at half maximum (FWHM) as the particle size increased. To evaluate the photocurrent conversion efficiency, we carried out incident photon-to-current efficiency (IPCE) measurements on all Au-NP/Ga_2O_3 photoelectrodes, as shown in Fig. 1b. Clear peaks were observed at approximately 580 nm in the IPCE action spectra of all Au-NPs/Ga_2O_3 photoelectrodes, and no detectable photo-response was obtained on the Ga_2O_3 photoelectrode without Au-NPs (see purple plot in Fig. 1b) in the visible wavelength region. In the case of Au-NP/Ga_2O_3 photoelectrodes loaded with small particles (≤15 nm), the IPCE band closely corresponded with the extinction spectrum of Au-NPs, indicating that the photocurrent was generated by the LSPR of Au-NPs.[13] The 15 nm Au-NP-loaded Ga_2O_3 sample showed the best PEC performance with a peak IPCE value of 0.11% at 580 nm, as shown by the red curve in Fig. 1b. For the 10 nm Au-NP-loaded Ga_2O_3 sample, its low extinction value caused a lower IPCE than the 15 nm Au-NPs. In contrast, when the particle size became larger than 15 nm, the IPCEs decreased. A possible explanation for the observed decrease in IPCE was the LSPR decay mechanism. For large particles, instead of nonradiative decay, radiative decay becomes the main pathway for LSPR decay, which is unfavourable for electron–hole generation.[24,25] The near-field enhancement spectra obtained by FDTD calculations (Fig. S2†) show a clear tendency that the large Au-NPs loaded on the Ga_2O_3 sample exhibited broadening of the LSPR peak, which was consistent with the extinction spectra. This broadening indicated a short dephasing time of LSPR due to significant radiation damping. Conclusively, Au-NPs/Ga_2O_3 with a particle size of 15 nm was the optimized photoelectrode for PEC photocurrent generation at visible wavelengths, and it was used in the following investigation.

To further improve the water oxidation ability of Au-NPs/Ga_2O_3, an interfacial modification was conducted by the introduction of a thin TiO_2 layer, which has a high hole-trapping ability. Because the CB alignment of TiO_2 is much more positive than that of Ga_2O_3, electrons cannot efficiently transfer from the CB of TiO_2 to that of Ga_2O_3.[3] Therefore, a thin TiO_2 layer was deposited on Au-NPs/Ga_2O_3 as the final layer, as shown in Fig. S3,† to maintain direct contact between the Au-NPs and Ga_2O_3 and to provide effective charge separation. Moreover, Au-NPs were partially inlaid in the TiO_2 layer (inset in Fig. 2b) without destroying the direct contact between the Au-NPs and Ga_2O_3 by the reported ALD procedure of TiO_2.[19]
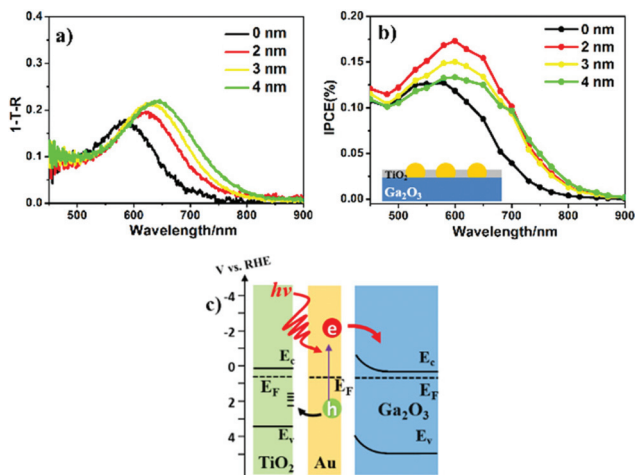
Fig. 2 (a) Absorption spectra and (b) IPCE action spectra of Au-NPs/Ga$_2$O$_3$ modified with different thicknesses of TiO$_2$. Inset: Cross-sectional schematic of TiO$_2$/Au-NPs/Ga$_2$O$_3$. (c) Schematic energy diagram showing the charge transfer in TiO$_2$/Au-NPs/Ga$_2$O$_3$.

With this structure, the plasmon-induced electrons could transfer from Au-NPs to Ga$_2$O$_3$ at the interface of Au-NPs/Ga$_2$O$_3$, and the hot holes could be captured at the surface states of TiO$_2$, which might accelerate the water oxidation reaction. As a control experiment, TiO$_2$ was deposited between the Au-NPs and Ga$_2$O$_3$. However, this arrangement was unfavourable for plasmon-induced charge separation, as discussed in detail in Fig. S6.†

The photoanodes of Au-NPs/Ga$_2$O$_3$ with various thicknesses of the TiO$_2$ modification layer (x-nm-TiO$_2$/Au-NPs/Ga$_2$O$_3$, where x = 2–4) were investigated in the following section. The thickness of TiO$_2$ was precisely controlled by controlling the number of ALD cycles from 40 to 80. According to the XRD measurements in Fig. S4a,† all peaks measured from 10° to 70° show almost the same diffraction angle and width, indicating the same crystallinity of Ga$_2$O$_3$ before and after TiO$_2$ deposition. The bandgap (4.8 eV) of Ga$_2$O$_3$ estimated from the Tauc plots in Fig. S4b† kept the same before and after the deposition of TiO$_2$. We also checked the elements oxidation states by XPS as shown in Fig. S5.† Ti 2p signal was presented after the deposition of TiO$_2$. The new signal of Ti 2p provided the direct evidence of the TiO$_2$ deposition on Ga$_2$O$_3$.[26] The binding energy of O 1s peak showed slightly broadening at the lower energy side rather than peak energy shift, which is ascribed to the presence of O 1s peak of Ti–O (529.8 eV) after TiO$_2$ deposition.[27] Additionally, the binding energy and the width of Ga 2p did not change after TiO$_2$ deposition. Based on the results above, it could be concluded that the crystallinity and band structure of Ga$_2$O$_3$ did not change after the deposition of TiO$_2$. According to the top-view SEM in Fig. S7,† after the deposition of TiO$_2$, the comparison of the morphology and particle size (d_{mean} ~ 15 nm) of Au-NPs before and after the deposition of the TiO$_2$ modification layer indicated that the ALD process at 300 °C barely affected the morphology of Au-NPs on Ga$_2$O$_3$.

Light absorption and carrier separation are two main factors contributing to photocurrent generation. To directly study the relationship between light absorption and PEC properties, the absorption spectrum of Au-NPs was calculated as the difference between the $(1 - T - R)$ spectrum of substrate with Au-NPs and without Au-NPs in Fig. 2a, where T and R are the transmission and reflection, respectively. Since the particle size and distribution of Au-NPs were similar, the red-shift of the peak position of the LSPR band from 585 to 645 nm was mainly caused by the refractive index increase in the surrounding media after TiO$_2$ deposition.[25] In addition, the absorption value at the LSPR peak also increased as the thickness of the TiO$_2$ layer increased. In contrast, the absorption at wavelengths shorter than 550 nm maintained almost the same value, which was only determined by the interband transition of Au.[19] The PEC performance of these modified samples is presented in Fig. 2b, and all the TiO$_2$/Au-NPs/Ga$_2$O$_3$ photoelectrodes show an IPCE increase in the visible region compared with that of the Au-NPs/Ga$_2$O$_3$ photoelectrode. Notably, 2-nm-TiO$_2$/Au-NPs/Ga$_2$O$_3$ showed the maximum IPCE value, which reached 0.17% at approximately 600 nm. Moreover, the stable photocurrent under 600 nm irradiation was approximately 1.5 times larger than that of Au-NPs/Ga$_2$O$_3$, as shown in Fig. S8.† The photocurrent of 2-nm-TiO$_2$/Au-NPs/Ga$_2$O$_3$ also showed a good stability because the photocurrent after 7.5 hours irradiation maintained 90% of the initial value of quasi-steady photocurrent, as shown in Fig. S9.†This result indicated that the interfacial modification by TiO$_2$ was beneficial for improving the PEC performance of Au-NPs/Ga$_2$O$_3$. Notably, after comparing the 2-nm-TiO$_2$/Au-NPs/Ga$_2$O$_3$ and pristine Au-NPs/Ga$_2$O$_3$, the IPCE peak of 2-nm-TiO$_2$/Au-NPs/Ga$_2$O$_3$ increased by 1.5 times, while the absorption increased by only 1.1 times at the peak LSPR wavelength. We suspect that much better charge separation occurred at the interface, resulting from the good hole-capturing ability of TiO$_2$, which was an important factor for IPCE enhancement, as depicted in Fig. 2c. After the deposition of TiO$_2$, the surface states of TiO$_2$ efficiently capture the plasmon-induced holes for efficient water oxidation. Moreover, the hot electrons generated at the Au-NPs/Ga$_2$O$_3$ interface could be smoothly transferred to the CB of Ga$_2$O$_3$ due to the direct contact between Au and Ga$_2$O$_3$. Based on this mechanism, hot carriers should have enough energy to achieve the hot-electron injection and water oxidation. The flat-band potential of 2-nm-TiO$_2$/Au-NPs/Ga$_2$O$_3$ was estimated to be −0.80 V vs. RHE after the deposition of 2 nm TiO$_2$ as shown in Fig. S10a.† The energy barrier between the flat-band potential of Ga$_2$O$_3$ for hot-electron injection and the oxidation potential of water (+1.23 V vs. RHE) is estimated as 2.03 eV (610 nm). Therefore, under the irradiation of light with the wavelength of 600 nm which is the peak wavelength of the IPCE action spectrum in Fig. 2b, both hot-electron injection and water oxidation can be achieved simultaneously.

As shown in Fig. 2a and b, the redshift of the TiO$_2$/Au-NPs/Ga$_2$O$_3$ IPCE peaks is not as obvious as their redshift in the absorption spectra. This observation could be explained by the threshold of photon energy needed for exciting electron/hole

separation at the Au-NPs/Ga$_2$O$_3$ interface, as discussed in Fig. S10.† This result suggested another insight, in that the electron injected into the CB of Ga$_2$O$_3$ had a high negative potential energy. The energy generated under light irradiation at 600 nm on the Ga$_2$O$_3$ photoanode, η_{photo}, was evaluated by being compared to an ideally nonpolarizable dark electrode as expressed in formula (1)

$$\eta_{photo} = \frac{I_{max}(1.23\,\mathrm{V}\,vs.\,\mathrm{RHE} - V_{max})}{P_{in}} \times 100 (\%) \qquad (1)$$

where I_{max} and V_{max} are the maximum output current and voltage, which generate the maximum electric power, respectively. P_{in} is the incident light intensity.[28]

The value of η_{photo} is the thermodynamic energy-conversion efficiency of the photoelectrode, and the η_{photo} value for 2-nm-TiO$_2$/Au-NPs/Ga$_2$O$_3$ under light irradiation at 600 nm was calculated as 0.06% from the I–V characteristics shown in Fig. S11.† This value was approximately twice as large as that of the Au-NPs/TiO$_2$-thin film (0.03%) due to the extremely negative onset potential. Therefore, the plasmonic Ga$_2$O$_3$ photoanode modified with the thin TiO$_2$ layer could simultaneously achieve water oxidation and hot-electron injection with a negative reduction potential under visible light irradiation.

To further verify the hole-trapping ability of the TiO$_2$ layer, the IPCE values of 2-nm-TiO$_2$/Au-NPs/Ga$_2$O$_3$ and Au-NPs/Ga$_2$O$_3$ were measured in an electrolyte with triethanolamine (TEOA), as shown in Fig. 3. TEOA is a sacrificial hole scavenger due to its fast reaction kinetics based on one-electron oxidation.[29] For Au-NPs/Ga$_2$O$_3$ without TiO$_2$ modification, the oxidation reaction with water by holes was difficult, as discussed above. The addition of TEOA dramatically increased the oxidation reactivity even though the hole-trapping ability of the Ga$_2$O$_3$ surface was poor, as illustrated in Fig. S12a.† The high IPCE of 2-nm-TiO$_2$/Au-NPs/Ga$_2$O$_3$ without TEOA in Fig. 3b indicated that the hot holes trapped at the surface states of 2-nm-TiO$_2$/Au-NPs/Ga$_2$O$_3$ oxidized water efficiently without the addition of TEOA, as shown in Fig. S12b.† Although the hole-trapping ability of TiO$_2$ could improve the oxidation reactivity and charge separation, the positive effect of interfacial modification on the IPCE showed a dependence on the thickness of TiO$_2$. When the TiO$_2$ thickness was larger than 2 nm, the IPCE improvement decreased even though the
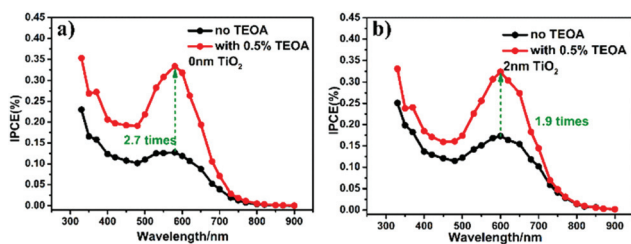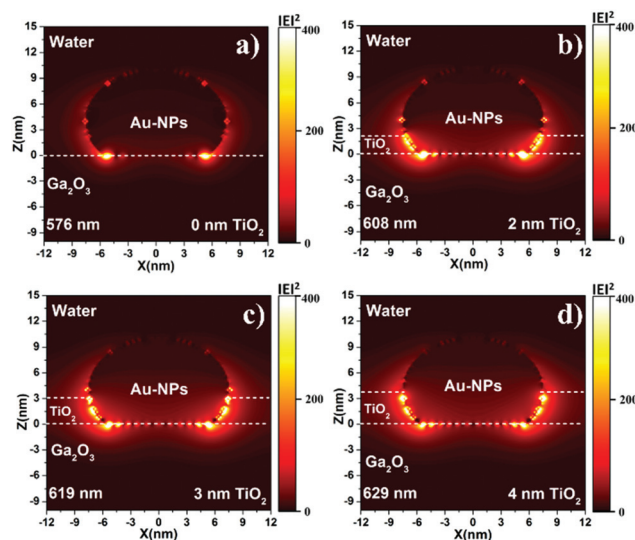

Fig. 4 Near-field distributions of Au-NPs/Ga$_2$O$_3$ modified with (a) 0, (b) 2, (c) 3, and (d) 4 nm TiO$_2$ layers, which was calculated by an FDTD simulation.

absorption increased. To understand the PEC performance difference of TiO$_2$/Au-NPs/Ga$_2$O$_3$ with different thicknesses of the TiO$_2$ layer, the near-field distribution at the interface of TiO$_2$/Au-NPs/Ga$_2$O$_3$ that determined the plasmon-induced carrier generation was calculated by a finite-difference time-domain (FDTD) simulation (Fig. 4). For Au-NPs/Ga$_2$O$_3$, the hot spot of the near-field was located at the interface between Au-NPs and Ga$_2$O$_3$, which are represented as the two bright spots in Fig. 4a. Regarding 2-nm-TiO$_2$/Au-NPs/Ga$_2$O$_3$, the near-field intensity was enhanced at the three-phase boundary of TiO$_2$/Au-NPs/Ga$_2$O$_3$ (Fig. 4b). However, the near-field intensity at the three-phase boundary decreased as the TiO$_2$ thickness increased (Fig. 4c and d). Though the near-field became stronger at the interface of TiO$_2$/Au-NPs with increasing distance from the Ga$_2$O$_3$ surface in Fig. 4c and d, the carriers generated at the Au-NPs/TiO$_2$ interface and then injected into the CB of TiO$_2$ contributed less to the IPCE, as discussed in Fig. S6.† Moreover, trapped holes at the three-phase boundary should migrate to the surface to participate in the water oxidation reaction. The thick TiO$_2$ modification layer would also suppress hole migration to the surface because of the extended path. Consequently, 2-nm TiO$_2$ interfacial-modified Au-NPs/Ga$_2$O$_3$ showed the best PEC improvement.

Conclusions

We demonstrated plasmon-induced photocurrent generation on wide bandgap Ga$_2$O$_3$ under visible light irradiation. The IPCE of Au-NPs/Ga$_2$O$_3$ was improved by an interfacial modification consisting of the deposition of a TiO$_2$ layer, which exhibits a high hole-trapping ability. The partial inlaying of Au-NPs with the TiO$_2$ layer could be beneficial for trapping plasmon-induced holes at the interfacial boundary between Au-NPs and

Fig. 3 IPCE action spectra of (a) Au-NPs/Ga$_2$O$_3$ and (b) 2-nm-TiO$_2$/Au-NPs/Ga$_2$O$_3$ measured in a KClO$_4$ aqueous solution with and without TEOA.

TiO$_2$ and improving the oxidation reactivity while maintaining efficient electron transfer. The 2-nm-thick TiO$_2$ interfacial modification shows up to a 1.5-times higher IPCE in the visible region than that without TiO$_2$. The thermodynamic energy-conversion efficiency for the 2-nm-TiO$_2$/Au-NPs/Ga$_2$O$_3$ photoelectrode under light irradiation at 600 nm was approximately twice as large as that of the Au-NPs/TiO$_2$-thin film due to the extremely negative onset potential.

Based on the above observations, the plasmonic Ga$_2$O$_3$ photoanode with the interfacial modification of a thin TiO$_2$ layer could demonstrate both a high ability for reduction, such as H$_2$ evolution, and oxidation ability for water oxidation because of the negative CB of Ga$_2$O$_3$ and the hole-trapping property of TiO$_2$, respectively. We believe this interfacial modification has enormous potential for use in artificial photosynthesis and could be applied in various fields and devices for photon energy conversion through structural optimization.

Materials and methods

Sample fabrication and structure characterization

The Sn-doped single-crystal β-Ga$_2$O$_3$ wafer (Novel Crystal Technology, Inc.) with an orientation of (−201) was cut to a size of 9.0 × 9.0 × 0.7 mm^3. These Ga$_2$O$_3$ substrates were successively rinsed with acetone and methanol in an ultrasonic bath for 5 min each. To fabricate Au-NPs on the surface of Ga$_2$O$_3$, a thin gold layer was deposited onto the substrates by electron-beam evaporation at room temperature. The deposition pressure was approximately 2.0 × 10^{-6} Pa, and the evaporation rate was set to approximately 0.16 Å s^{-1}. Subsequently, the samples were annealed in air at 800 °C for 1 h. The fabrication processes are shown in Fig. S3 in the ESI.† The particle size of Au-NPs was controlled by changing the thickness of the Au film. The TiO$_2$ layer was deposited by a commercial hot-wall flow-type ALD reactor (SUNALETM R series, Picosun, Finland) at 300 °C with a deposition rate of 0.05 nm per cycle. TiCl$_4$ and deionized water vapor were used as the Ti and O sources, and N$_2$ was used as the carrier gas and purge gas. The pulse time and purge time were set as 0.1 and 4.0 s, respectively. X-Ray diffraction chart was applied to check the phase structure of Ga$_2$O$_3$ by RIGAKU RINT-2000/PC using Cu Kα radiation. The valence of Ga, Ti and O was measured by an X-ray photoelectron spectrometer (XPS, JPS-9200, JEOL).

Optical properties and morphology characterization

A photonic multichannel analyser (PMA C7473, Hamamatsu Photonics) system was applied to measure the optical reflectance and transmittance spectra. Bandgap of Ga$_2$O$_3$ was estimated by the Tauc plots obtained from the transmittance spectra measured by A UV-Vis spectrophotometer (UV-3100PC, SHIMADZU). The surface morphology was identified by field-emission scanning electron microscopy (FE-SEM, JSM-6700FT, JEOL) with a maximum resolution of 1 nm. Additionally, ImageJ software was used to analyse the mean particle size.

Photoelectrochemical measurement

To obtain the ohmic contact, an In–Ga alloy with a weight ratio of 4 : 1 was coated on the backside and sidewall of the Au-NPs/Ga$_2$O$_3$ substrates. Then, the samples were connected to a copper plate in a Teflon reaction cell, which was connected to an electrochemical analyser (ALS/CH Instruments 852C, ALS) with a copper lead wire. The irradiation window consisted of a pinhole with a diameter of 2.0 mm on the lid of the cell. A three-electrode system consisting of a platinum wire and a saturated calomel electrode (SCE) as the counter electrode and reference electrode, respectively, was applied to measure the PEC properties. In addition, a 0.1 M KClO$_4$ aqueous solution without an electron donor was used as the electrolyte. During the photocurrent measurement, a potential of +0.3 V vs. SCE was applied to the working photoelectrode. The IPCE was calculated by formula (2):

$$\text{IPCE}(\lambda) = \frac{1240 \times I(\text{A cm}^{-2})}{\lambda(\text{nm}) \times P_{\text{in}}(\text{W cm}^{-2})} \quad (2)$$

where I is the photocurrent density, λ is the wavelength of incident light and P_{in} is the incident light intensity. In addition, Mott–Schottky experiments were carried out at a constant frequency of 5000 Hz in a scan window of −1.5 to 1.0 V vs. SCE in the three-electrode system described above.

Numerical simulations

Full-field electromagnetic wave simulations were performed using the FDTD method (FDTD Solutions, Lumerical). The investigated structure was simulated using perfectly matched layers along the z-direction and periodic boundary conditions along the x- and y-directions with a period of 20 nm. An ellipsoid sphere with a diameter of 15 nm in the x and y directions and 10 nm in the z direction was used to model the Au-NPs. In the simulation, the refractive index of Au was taken from the optical constants of Johnson and Christy. Ga$_2$O$_3$ and TiO$_2$ were treated as dielectric materials with refractive indices of 1.8 and 2.4, respectively.

Conflicts of interest

There are no conflicts to declare.

Acknowledgements

Notes and references

1 L. Ni, M. Tanabe and H. Irie, *Chem. Commun.*, 2013, **49**, 10094–10096.

2 K. Maeda and K. Domen, *J. Phys. Chem. C*, 2007, **111**, 7851–7861.

3 M. Navarrete, S. Cipagauta-Díaz and R. Gómez, *J. Chem. Technol. Biotechnol.*, 2019, **94**, 3457–3465.

4 Y. Sakata, Y. Matsuda, T. Nakagawa, R. Yasunaga, H. Imamura and K. Teramura, *ChemSusChem*, 2011, **4**, 181–184.

5 Y. Sakata, T. Nakagawa, Y. Nagamatsu, Y. Matsuda, R. Yasunaga, E. Nakao and H. Imamura, *J. Catal.*, 2014, **310**, 45–50.

6 Y. Hou, X. Wang, L. Wu, Z. Ding and X. Fu, *Environ. Sci. Technol.*, 2006, **40**, 5799–5803.

7 H. Tsuneoka, K. Teramura, T. Shishido and T. Tanaka, *J. Phys. Chem. C*, 2010, **114**, 8892–8898.

8 T. Oshima, K. Kaminaga, H. Mashiko, A. Mukai, K. Sasaki, T. Masui, A. Kuramata, S. Yamakoshi and A. Ohtomo, *Jpn. J. Appl. Phys.*, 2013, 52.

9 A. Kudo and I. Mikami, *J. Chem. Soc., Faraday Trans.*, 1998, **94**, 2929–2932.

10 H. Kong, H. Li, G. Lin and H. Zhang, *Catal. Lett.*, 2011, **141**, 886–894.

11 Y. Sakata, Y. Matsuda, T. Yanagida, K. Hirata, H. Imamura and K. Teramura, *Catal. Lett.*, 2008, **125**, 22–26.

12 T. Yanagida, Y. Sakata and H. Imamura, *Chem. Lett.*, 2004, **33**, 726–727.

13 X. Shi, K. Ueno, T. Oshikiri and H. Misawa, *J. Phys. Chem. C*, 2013, **117**, 24733–24739.

14 Z. Zheng, W. Xie, B. Huang and Y. Dai, *Chem. – Eur. J.*, 2018, **24**, 18322–18333.

15 A. Abdalla, I. Khan, M. Sohail and A. Qurashi, *Sol. Energy*, 2019, **181**, 333–338.

16 X. Ma, Y. Dai, L. Yu and B. Huang, *Light: Sci. Appl.*, 2016, **5**, e16017.

17 K. Wu, J. Chen, J. McBride and T. Lian, *Science*, 2015, **349**, 632–635.

18 C. Clavero, *Nat. Photonics*, 2014, **8**, 95–103.

19 X. Shi, K. Ueno, T. Oshikiri, Q. Sun, K. Sasaki and H. Misawa, *Nat. Nanotechnol.*, 2018, **13**, 953–958.

20 X. Shi, X. Li, T. Toda, T. Oshikiri, K. Ueno, K. Suzuki, K. Murakoshi and H. Misawa, *ACS Appl. Energy Mater.*, 2020, **3**, 5675–5683.

21 K. Suzuki, X. Li, Y. Wang, F. Nagasawa and K. Murakoshi, *ACS Energy Lett.*, 2020, **5**, 1252–1259.

22 S. Bera, J. Lee, S. Rawal and W. Lee, *Appl. Catal., B*, 2016, **199**, 55–63.

23 P. Reineck, D. Brick, P. Mulvaney and U. Bach, *J. Phys. Chem. Lett.*, 2016, **7**, 4137–4141.

24 R. Sundararaman, P. Narang, A. Jermyn, W. Goddard and H. Atwater, *Nat. Commun.*, 2014, **5**, 5788.

25 C. Sonnichsen, T. Franzl, T. Wilk, G. von Plessen, J. Feldmann, O. Wilson and P. Mulvaney, *Phys. Rev. Lett.*, 2002, **88**, 077402.

26 M. Warwick, G. Carraro, E. Toniato, A. Gasparotto and C. Maccato, *Surf. Sci. Spectra*, 2016, **23**, 61–69.

27 B. Bharti, S. Kumar, H. Lee and R. Kumar, *Sci. Rep.*, 2016, **6**, 323.

28 R. Coridan, A. Nielander, S. Francis, M. McDowell, V. Dix, S. Chatman and N. Lewis, *Energy Environ. Sci.*, 2015, **8**, 2886–2901.

29 Y. Pellegrin and F. Odobel, *C. R. Chim.*, 2017, **20**, 283–295.